

Modeling Defect-Level Switching for Highly-Nonlinear and Hysteretic Electronic Devices

Jiahao Dong and R. Jaramillo*

Department of Materials Science and Engineering, Massachusetts Institute of Technology,
Cambridge, MA 02139, USA

* Corresponding author: rjaramil@mit.edu

Abstract

Many semiconductors feature defects with charge state transition levels that can switch due to structure changes following defect ionization: we call this defect-level switching (DLS). For example, DX centers in III-V compounds, and oxygen vacancies in ZnO, can switch between deep and shallow donor configurations, and these bistable dynamics are responsible for persistent photoconductivity. We recently demonstrated highly-nonlinear, hysteretic, two-terminal electronic devices using DLS in CdS [H. Yin, A. Kumar, J.M. LeBeau, and R. Jaramillo, *Phys. Rev. Applied* **15**, 014014 (2021).] The resulting devices operate without mass transport, and in the opposite sense to most resistive switches: they are in a high-conductivity state at equilibrium, and switch to a low-conductivity state at forward bias. Although DLS uses the same defect transitions that are responsible for persistent photoconductivity, DLS devices operate without light and can be orders-of-magnitude faster due to exponential tuning of transition rates with voltage. In this work we use theory and numerical simulation to explore the design space of DLS devices, emphasizing the tradeoff between speed and on/off ratio. Our results will be useful to guide future applications of these unusual devices.

1. Introduction

Nonlinear and hysteretic two-terminal semiconductor devices are required for many applications including circuit protection, oscillators, and emerging concepts for computing. For computing, resistive switching is a key functionality in many devices proposed for storage-class memory, compute-in-memory, and approaches to neuromorphic data processing that move beyond the CMOS digital logic paradigm. Broadly speaking, there are several classes of resistive switching technologies: those based on mass transport, those based on phase transformations, and those based on magnetic phenomena. We recently proposed and demonstrated a mechanism for resistive switching based on charge trapping and de-trapping at point defects that exhibit bi-stable lattice configurations, causing them to switch between deep and shallow donor states; we termed this effect defect level switching (DLS).¹ Bi-stability produces nonlinear and hysteretic behavior, but DLS devices operate without mass transport or phase transformations. The devices that we experimentally demonstrated are based on CdS/MoO₃ heterojunctions and exhibit unusual behavior: they are in a low-resistivity state at equilibrium, and switch to a high-resistivity state under forward bias. The devices are bipolar and return to low-resistivity under reverse bias. This behavior – transient switching of an *n*-type material to a high-resistance state upon electron injection – recalls the operation of Gunn diodes that are the basis for high-frequency oscillators, although the physical mechanism is different.

The CdS/MoO₃ devices that we demonstrated are volatile and have potential applications in computing paradigms that involve analog signals and dynamical networks. For instance, DLS devices are highly nonlinear dynamical systems and can be used in physical reservoir computing, which can achieve fast information processing with low cost-of-learning.² The resistive state decay rate varies exponentially with applied bias, offering a rich set of dynamics. Further, being based on point defect ionization without mass transport or collective phase transformations means that DLS devices can be free from cycle-to-cycle variation, and may offer long-term reliability superior to other resistive switching technologies. Being based on the physics of semiconductor point defects, DLS devices are amenable to technology computer-aided design (TCAD), perhaps more so than resistive switches based on nanoscale mass transport and phase transformations. DLS devices may also make possible inverse device design, wherein the desired dynamical response is determined from design processes at the higher levels of circuits, systems, and algorithms, and then realized at the device level by data-driven selection of semiconductor materials and point defects. DLS phenomena is already established in a number of compound semiconductors including AlGaAs, III-nitrides, ZnO, CuInSe₂, CuGaSe₂, and CdS, suggesting a wide solid-state chemistry design space that could be explored computationally.^{3–7}

With such future outcomes in mind, here we develop numerical simulations to explore the performance space of DLS devices. We describe the fundamental mechanism by which DLS phenomena controls device conductivity. We parameterize the switching performance of a generic DLS device, and we predict experimentally-accessible operating regimes for parameters representative of several materials of interest. Our work here includes direct and thermally-assisted defect-to-band transitions, and band-to-band tunneling. In this work we model only majority-carrier transport; in future work we will consider defect-to-band tunneling, which can introduce minority carrier effects.

Schroeder *et al.* in 2010 published a numerical study of the tradeoff between access voltage and retention time for resistive switching memory based on charge trapping and detrapping at point defects.⁸ The results reported here can be viewed an extension of this earlier work, to the case of bistable defects. However, our focus is on performance parameters relevant to oscillators and other non-volatile devices, instead of on memory. We also introduce substantial new developments in semiconductor device modeling, necessary to efficiently simulate the performance of junctions with bistable defects, which were not considered in the earlier work.

2. Effect of DLS on the depletion region and conductivity of a Schottky heterojunction

DLS phenomena can produce resistive switching through the mechanism of photoconductivity (*i.e.* a photoresistor), or through interaction with a semiconductor heterojunction without the influence of light. Our focus is on this latter category, in which the conductivity of a heterojunction undergoes hysteretic and nonlinear switching due to DLS without illumination, as realized experimentally in our earlier work.¹ When a defect can switch between deep and shallow donor configurations, the concentrations of deep and shallow donors become dynamical variables that depend on position and time. These defect concentrations affect the size and shape of the depletion region, at a Schottky junction for instance, which affect the junction conductivity. DLS-active levels typically have long relaxation times, leading to persistence and hysteretic behavior. The

timescale of switching can be accelerated exponentially with voltage applied to the junction. This makes the dynamics and behavior of DLS-based heterojunction devices faster and more diverse than simple photoresistors, not to mention more amenable to integration in microelectronics, because there is no need for controlled illumination.

We focus in this work on DLS phenomena in *n*-type materials. Examples include DX centers in *n*-AlGaAs, and anion vacancies in ZnO and CdS.^{3–6} DX centers are thus named because they were thought to involve a donor (typically Si) paired with an unknown point defect (it is now believed that DX centers are lone substitutional dopants).⁹ DX centers have long been a nuisance for III-V device technology because the DLS phenomenon limits achievable shallow donor density.^{7,9} DLS phenomena are also found in *p*-type semiconductors including CuInSe₂ and CuGaSe₂.⁵

We construct a generic model of the effect of DLS on a metal-semiconductor heterojunction. We present the semiconductor energy level diagram in **Fig. 1a**. The metastable defect is a double donor exhibiting negative-*U* phenomena.⁵ We represent the neutral, deep donor as V_{An}^{\times} , and the doubly-ionized, shallow donor as $(V_{\text{An}}^{\bullet\bullet})^*$. The Kröger-Vink notation is representative of an anion vacancy, appropriate for ZnO and CdS, and the asterisk indicates the change in lattice configuration in the shallow donor configuration, illustrated schematically in **Fig. 1b**. The charge transition energy level is E_{deep} and E_{shallow} in the deep- and shallow-donor configurations, respectively. In **Fig. 1a** we draw E_{shallow} above the conduction band edge, E_{C} , as computed for the case of ZnO.⁵ However, for the work here it is important only that this be a shallow donor level, and it can be either above or below E_{C} without affecting the results here (the position of E_{shallow} vis-à-vis the conduction band edge does have implications for the metastable state stability).

The transition rate between V_{An}^{\times} and $(V_{\text{An}}^{\bullet\bullet})^*$ depends on the difference between the Fermi energy (E_{F}) and a transition energy level that we label E_{trans} (see Appendix, Eqn. A6). In the bulk, E_{F} is above E_{trans} and thermal equilibrium favors the V_{An}^{\times} configuration. However, when E_{F} is below E_{trans} , such as can occur at a heterojunction, thermal equilibrium favors $(V_{\text{An}}^{\bullet\bullet})^*$. The energy levels of shallow and deep donors are labeled as E_{shallow} (corresponding to the $(V_{\text{An}}^{\bullet})^*/(V_{\text{An}}^{\bullet\bullet})^*$ transition) and E_{deep} (corresponding to the $V_{\text{An}}^{\times}/V_{\text{An}}^{\bullet}$ transition), respectively.

Band bending at a metal-semiconductor heterojunction means that the V_{An}^{\times} -to- $(V_{\text{An}}^{\bullet\bullet})^*$ transition depends on space and time. The shallow donor density becomes a dynamical variable, and the shape and size of the depletion region becomes non-trivial and hysteretic with applied bias. This makes the junction conductivity hysteretic with applied bias, which manifests as resistive switching. In this work we consider only the DLS-active defects, and not the effects of other defects in the bulk or at the interface. The following analysis is similar to that developed for capacitance-voltage (*C-V*) profiling and deep level transient spectroscopy (DLTS), with the distinctions that we focus on junction conductivity (not capacitance), and that we emphasize the use of DLS phenomena to realize heterojunction devices with new functionality, instead of using heterojunctions for defect spectroscopy as in DLTS.¹⁰

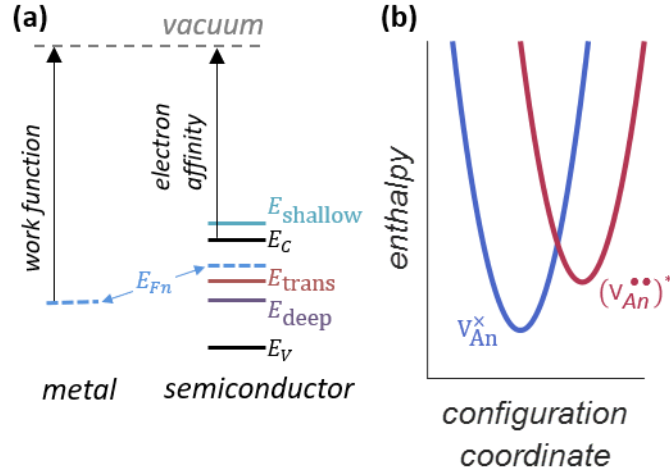


Figure 1: Schematic of heterojunction and DLS phenomena. (a) Materials used to make a DLS heterojunction device: a semiconductor with DLS-active defects (drawn here as n -type), and a metal or highly-doped semiconductor. Illustration shows the material energy levels before junction formation; terms are described in the text. A corresponding schematic could be drawn for a p -type semiconductor with DLS-active defects. (b) Schematic of system enthalpy vs. configuration coordinate for the defect in the neutral deep-donor configuration (V_{An}^x) and the doubly-ionized shallow-donor configuration ($(V_{An}^{..})^*$). The notation is suggestive of an anion vacancy; the metastable configuration is indicated by an asterisk (*). The configuration coordinate may for instance be a measure of bond lengths around the defect.

We consider three mechanisms for current transport across the Schottky junction: thermionic emission, diffusion, and tunneling. Thermionic emission depends only on the barrier height. In a Schottky junction, the barrier height is a constant, determined by the difference between metal work function and semiconductor electron affinity. Therefore, thermionic emission is independent of defect configurations in the depletion region and does not participate in resistive switching: the thermionic emission current density is not switched by DLS. The diffusion current varies with the inverse of the width of the depletion region, and therefore does depend on the state of DLS-active defects. The tunneling current is exponentially sensitive to the depletion width, and contributes most to resistive switching due to DLS. We model the tunneling current using thermionic field emission (TFE) theory, appropriate for devices at finite temperature. Key equations and derivations are presented in the Appendix.

To illustrate the effect of DLS on the depletion region and conductivity of a Schottky heterojunction, we simulate a device based on CdS, as in our earlier experimental work.¹ We use plausible values for the materials and interfaces, described in the Appendix. In order to make TFE the dominant current transport mechanism and thus have a large on/off resistive switching ratio, as observed experimentally, we set a relative high concentration of DLS-active defects to be $N_t = 5 \times 10^{18} \text{ cm}^{-3}$ (unless otherwise specified), which is an experimentally-realistic defect concentration. We present in **Fig. 2a-b** band diagrams for the heterojunction in the on (high conductivity) and off (low conductivity) states, respectively. In the on state, the DLS-active defects are in their shallow donor configuration throughout the depletion region. The ionized donor density

is high, and the depletion region is narrow. In the off state, the DLS-active defects undergo a transition from the shallow donor configuration to the deep donor configuration within the depletion region. As a result, the ionized donor density drops, causing the depletion region to elongate, visible in comparing **Fig. 2a-b**. The on / off states are defined by calculating thermal equilibrium for reverse bias of -0.3 V / forward bias of +0.3 V, respectively. We then fix these defect concentrations and simulate the band diagram at a forward bias of +0.1 V, as a typical low-voltage test condition.

For each configuration, there is a junction depth at which the concentrations of DLS-active defects in their shallow- and deep-donor configurations are equal. We call this position the cross point and denote it as $x_{X\text{-point}}$. The position $x_{X\text{-point}}$ determines the size and shape of the depletion region, which controls the junction conductivity. In the on state, **Fig. 2a**, $x_{X\text{-point}}$ (indicated by vertical dashed line) is farther from the junction, the depletion region is narrower, and the TFE current is enhanced (**Fig. 2d**). In the off state, **Fig. 2b**, $x_{X\text{-point}}$ is closer to the junction, the depletion region is wider, and the TFE current is suppressed. We illustrate in **Fig. 2c** the position of $x_{X\text{-point}}$ in the on and off states.

We present in **Fig. 2d** the thermionic emission, diffusion, and TFE current densities for the on and off states under a forward bias of +0.1 V. TFE is by far the current transport mechanism most sensitive to the depletion width, with a change in conductivity nearly two orders of magnitude in size, compared to only a 25% change for diffusion, and no change for thermionic emission.

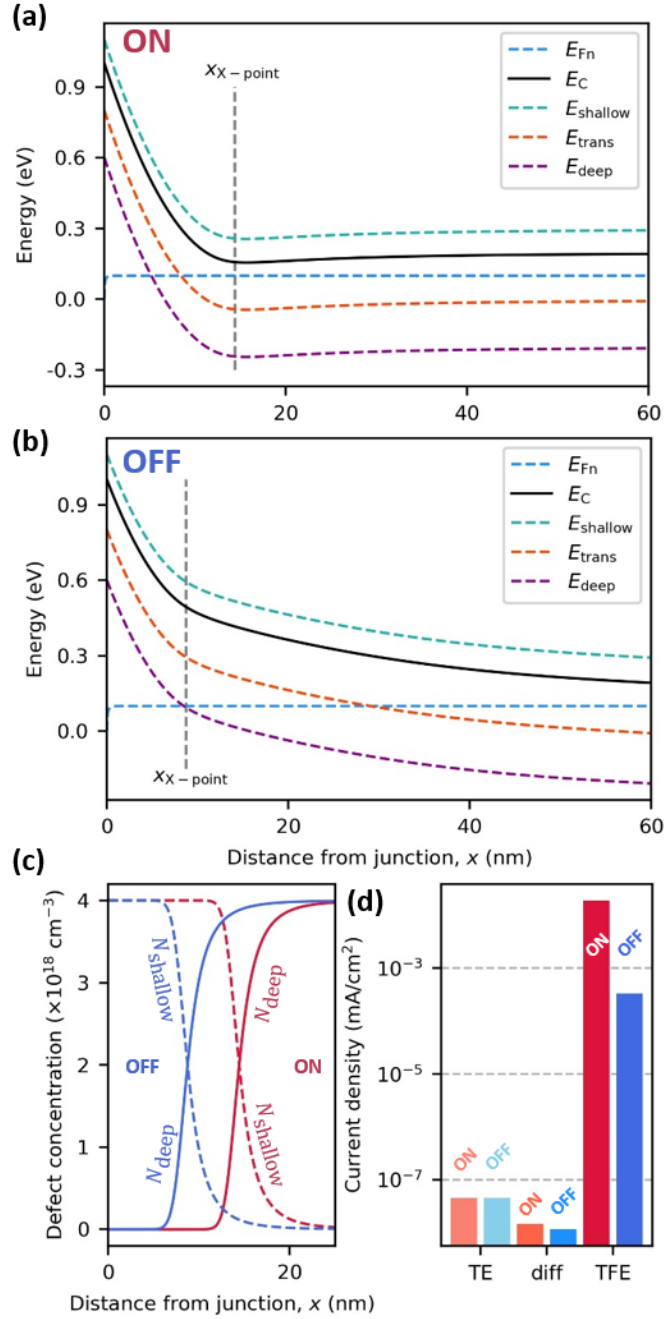


Figure 2: Effect of DLS on the depletion region and conductivity of a Schottky heterojunction, simulated for parameters typical of CdS. (a, b) Band diagrams for the semiconductor containing a DLS-active double donor in the on (a) and off (b) states. The semiconductor-metal junction is located at $x = 0$ nm, and the vertical dashed lines indicate the position of $x_{X\text{-point}}$. (c) Depth-dependence of concentrations of DLS-active defects in the deep and shallow donor configurations in the on and off states; we denote as $x_{X\text{-point}}$ the position at which the concentrations of deep and shallow donors cross. (d) Comparison of thermionic emission, diffusion, and thermionic field

emission (TFE) current densities in the on and off states; calculations for $N_t = 4 \times 10^{18} \text{ cm}^{-3}$ and $E_C - E_{\text{trans}} = 0.2 \text{ eV}$.

3. Modeling the dynamics of resistive switching in DLS device

The drive frequency and amplitude substantially influence the electrical behavior of DLS devices. The frequency dependence and hysteretic behavior stem from the fact that the lattice relaxations associated accompanying double electron capture and emission are not arbitrarily fast, and the depletion region is often out-of-equilibrium. The bandwidth for resistive switching shifts to higher frequency with increase in drive amplitude, due to exponential speedup.

We use a conventional model of double electron capture and emission, consistent with our understanding of DLS-active defects such as oxygen vacancies in ZnO (as illustrated in **Fig. 1**).¹² The study of carrier capture and emission processes is a rich field, particularly for defects with strong coupling between charge state and lattice configuration, and is beyond the scope of this work. The conventional model that we use here describes the physics with sufficient generality. A neutral deep donor transforms into a doubly-ionized shallow donor by emitting two electrons / capturing two holes, accompanied by a large lattice relaxation. Likewise, a doubly-ionized shallow donor transforms into a neutral deep donor by capturing two electrons/emitting two holes. The double electron/hole capture/emission rates are given by:

$$\tau_{EC}^{-1} = \frac{1}{\nu_{\text{phonon}}} \tau_{ec}^{-1} \tau_{ec}^{-1} \exp\left(-\frac{\Delta E_{EC}}{k_B T}\right) \quad (1)$$

$$\tau_{EE}^{-1} = \frac{1}{\nu_{\text{phonon}}} \tau_{ee}^{-1} \tau_{ee}^{-1} \exp\left(-\frac{\Delta E_{EE}}{k_B T}\right) \quad (2)$$

$$\tau_{HC}^{-1} = \frac{1}{\nu_{\text{phonon}}} \tau_{hc}^{-1} \tau_{hc}^{-1} \exp\left(-\frac{\Delta E_{HC}}{k_B T}\right) \quad (3)$$

$$\tau_{HE}^{-1} = \frac{1}{\nu_{\text{phonon}}} \tau_{he}^{-1} \tau_{he}^{-1} \exp\left(-\frac{\Delta E_{HE}}{k_B T}\right) \quad (4)$$

τ_{EC}^{-1} , τ_{EE}^{-1} , τ_{HC}^{-1} and τ_{HE}^{-1} are the rates of double electron capture, double electron emission, double hole capture, and double hole emission, respectively. ν_{phonon}^{-1} is an attempt frequency for the lattice relaxation. ΔE_{EC} , ΔE_{EE} , ΔE_{HE} and ΔE_{HC} are the activation energies for double electron capture, double electron emission, double hole emission and double hole capture, respectively. τ_{ec}^{-1} , τ_{ee}^{-1} , τ_{hc}^{-1} and τ_{he}^{-1} denote the rates of single electron capture, single electron emission, single hole capture, and single hole emission, respectively. These are given by:

$$\tau_{ec}^{-1} = \sigma v_{rms} n = \sigma v_{rms} N_C \exp\left(\frac{-E_C + E_{Fn}}{k_B T}\right), \quad \tau_{ee}^{-1} = \sigma v_{rms} N_C \quad (5)$$

$$\tau_{hc}^{-1} = \sigma v_{rms} p = \sigma v_{rms} N_V \exp\left(\frac{-E_{Fn} + E_V}{k_B T}\right), \quad \tau_{he}^{-1} = \sigma v_{rms} N_V \quad (6)$$

σ is the defect capture cross section, v_{rms} the thermal velocity of electrons/holes, n/p are the free electron/hole concentration, and N_C/N_V are the conduction/valence band effective density of states. E_{Fn} is the Fermi energy, which is equal to the applied voltage.

With time-varying bias, it is computationally very demanding to implement a full simulation and converge the time-varying band diagram at each step, capturing full details of electron capture and emission in space and time. Therefore, we have developed an approximate model that involves simulating the equation of motion of $x_{\text{X-point}}$ (see Appendix for details). As seen in **Fig. 2**, $x_{\text{X-point}}$ determines the size and shape of the depletion region, which controls the junction conductivity. We derived the following equation of motion for $x_{\text{X-point}}$, with which we can simulate the dynamics of the band diagram:

$$\frac{dx_{\text{X-point}}}{dt} \propto -\exp\left(-\frac{E_{\text{switch}}}{k_B T}\right) \sinh\left(\frac{2E_{Fn} - 2E_{Fn,TR}(x_{\text{X-point}})}{k_B T}\right) \quad (7)$$

E_{switch} denotes the characteristic energy of the kinetic transformation of metastable defects (Eqn. A5) and $E_{Fn,TR}(x_{\text{X-point}})$ the metastable transition energy level at the cross point. $E_{Fn,TR}$ has the same physical meaning as E_{trans} but $E_{Fn,TR}$ is depends on position through the heterojunction.

The motion of the cross point ($x_{\text{X-point}}$) follows the kinetics of defect charge trapping and detrapping, as local equilibrium is restored following a change in applied bias. The movement of $x_{\text{X-point}}$ is accelerated exponentially with applied bias, due to the hyperbolic sine function. This is the physical origin of the speedup in resistive switching in DLS devices compared to simple photoresistors: although both types of device may be based on the same functional defects, in DLS devices the rates of electron capture and emission vary exponentially with applied bias, as indicated by Eqn. (5) and (6).

For the sake of computational efficiency, we introduce an additional approximation to model the band diagram. Instead of smoothly-varying concentrations N_{shallow} and N_{deep} (as in **Fig. 2c**), we assume that they behave as step functions, changing abruptly at $x_{\text{X-point}}$: for a given value of $x_{\text{X-point}}$, we assume that $N_{\text{shallow}} = N_t$ for $x < x_{\text{X-point}}$, and $N_{\text{deep}} = N_t$ for $x > x_{\text{X-point}}$. With this approximation, the electric potential varies quadratically for $x < x_{\text{X-point}}$, linearly for $x > x_{\text{X-point}}$, and can be modeled in closed form. In **Fig. 3a** we compare the band structure according to this approximation, and that resulting from a full numerical solution, for a given value of $x_{\text{X-point}}$. The difference in electric potential is slight, and the difference in current density between the two cases is less than 3%.

Using the equation of motion of $x_{\text{X-point}}$ (Eqn. 7), and the simplifying assumption of a sharp change in N_{shallow} and N_{deep} , we can explore the parameter space of DLS dynamics with computational ease. In **Fig. 3b** we illustrate the dynamics with three snapshots in time. We start at t_1 with a band diagram at zero bias and at equilibrium. At t_2 the bias is instantaneously raised to +0.3 V. This flattens the conduction band and changes the relative position of E_F and E_{trans} , but the concentrations N_{shallow} and N_{deep} do not respond immediately, and $x_{\text{X-point}}$ remains at the same position (indicated by a red star). For $t > t_2$, shallow donors are transformed into deep donors by

double electron capture, and $x_{X\text{-point}}$ moves to the left. At a later time t_3 , the defects have reached local equilibrium, and $x_{X\text{-point}}$ has reached its new steady-state position $x_{X\text{-point}}^{\text{SS}}$ (indicated by a blue star). The junction resistivity increases by 357% from t_2 to t_3 as a result of the depletion region growing. In this way, the application of forward bias – which in a normal Schottky junction would increase the conductivity by approaching the flat-band condition – here decreases the conductivity.

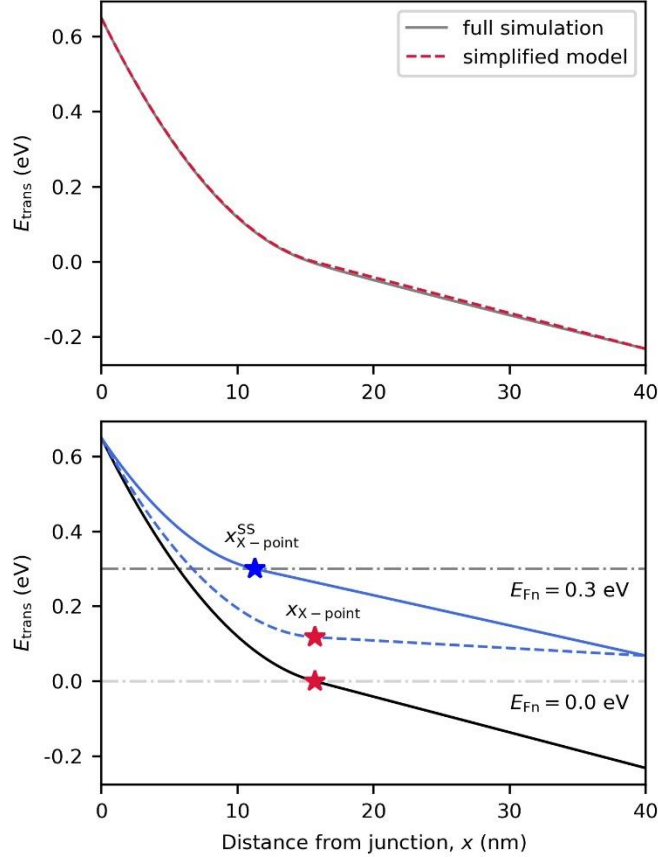


Figure 3: Evaluating a computationally-efficient theoretical model for the DLS device band diagram. (a) Steady-state energy band diagram at zero bias and as calculated with full numerical convergence, allowing the concentrations N_{shallow} and N_{deep} to vary continuously with position (grey solid line), compared to a simplified model in which N_{shallow} and N_{deep} change abruptly at $x_{X\text{-point}}$ (red dashed line). The simplified model is a very good approximation of the full solution. For simplicity we show only E_{trans} , which tracks the electric potential and has the same position-dependence as other energy levels. (b) Time progression of the band diagram during a resistive switching event; stars indicate $x_{X\text{-point}}$. Black solid line: initial time t_1 at zero bias and steady-state. Blue dashed line: time $t_2 > t_1$, at which the bias is raised instantaneously to +0.3 V. Blue solid line: time $t_3 > t_2$, by which time a population of defects have transformed from ionized shallow donors to neutral deep donors, moving $x_{X\text{-point}}$ to the new steady-state position $x_{X\text{-point}}^{\text{SS}}$, extending the depletion region, and reducing the junction conductivity. Calculations shown for $N_t = 4 \times 10^{18} \text{ cm}^{-3}$ and $E_C - E_{\text{trans}} = 0.2 \text{ eV}$.

The dynamics of hysteretic resistive switching are controlled by the rate at which $x_{\text{X-point}}$ moves to restore local equilibrium after a change in bias. In **Fig. 4a** we illustrate the near-linear dependence of the steady-state position $x_{\text{X-point}}^{\text{SS}}$ as the bias varies in time as a triangular wave with amplitude 0.4 V. In **Fig. 4b-c** we illustrate the simulated behavior of $x_{\text{X-point}}$ and current density for different drive frequencies. To demonstrate the frequency-dependence of DLS, we model low- (0.1 Hz), intermediate- (1 kHz) and high-frequency (10 MHz) response (this range can shift with material parameters). At low frequency, defects have sufficient time to reach local equilibrium as the bias changes, and $x_{\text{X-point}}$ closely tracks $x_{\text{X-point}}^{\text{SS}}$. We predict no hysteretic resistive switching at this drive frequency. At intermediate frequency, $x_{\text{X-point}}$ still exhibits a large oscillation but now lags $x_{\text{X-point}}^{\text{SS}}$ in time, which behavior we expect to produce hysteretic resistive switching with a large on/off ratio. Finally, at high frequency, the motion of $x_{\text{X-point}}$ is too slow to respond to applied bias and track $x_{\text{X-point}}^{\text{SS}}$, the oscillation amplitude of $x_{\text{X-point}}$ is reduced, and we expect the on/off conductivity ratio to be suppressed.

The amplitude of resistive switching (*i.e.*, the on/off conductivity ratio) depends on the change in the depletion region band diagram, and how this affects the current transport mechanisms. These dependencies can be summarized by frequency-response curves that represent the on/off ratio as a function of drive frequency for a fixed drive amplitude. In **Fig. 4d** we plot the on/off ratio of TFE current density at a bias of +0.1 V during one period of bias oscillation, as a function of drive frequency between 10^{-2} and 10^8 Hz, for drive amplitudes 0.3, 0.4, and 0.5 V. As expected from the above discussion, we see that the on/off ratio has a maximum at intermediate frequencies. Increasing the drive amplitude increases the on/off ratio. This is expected because the width of sample within which defects undergo level switching increases with drive voltage. We also see that increasing drive amplitude increases the device bandwidth, enabling higher-frequency operation, exceeding 100 MHz for 0.5 V drive.

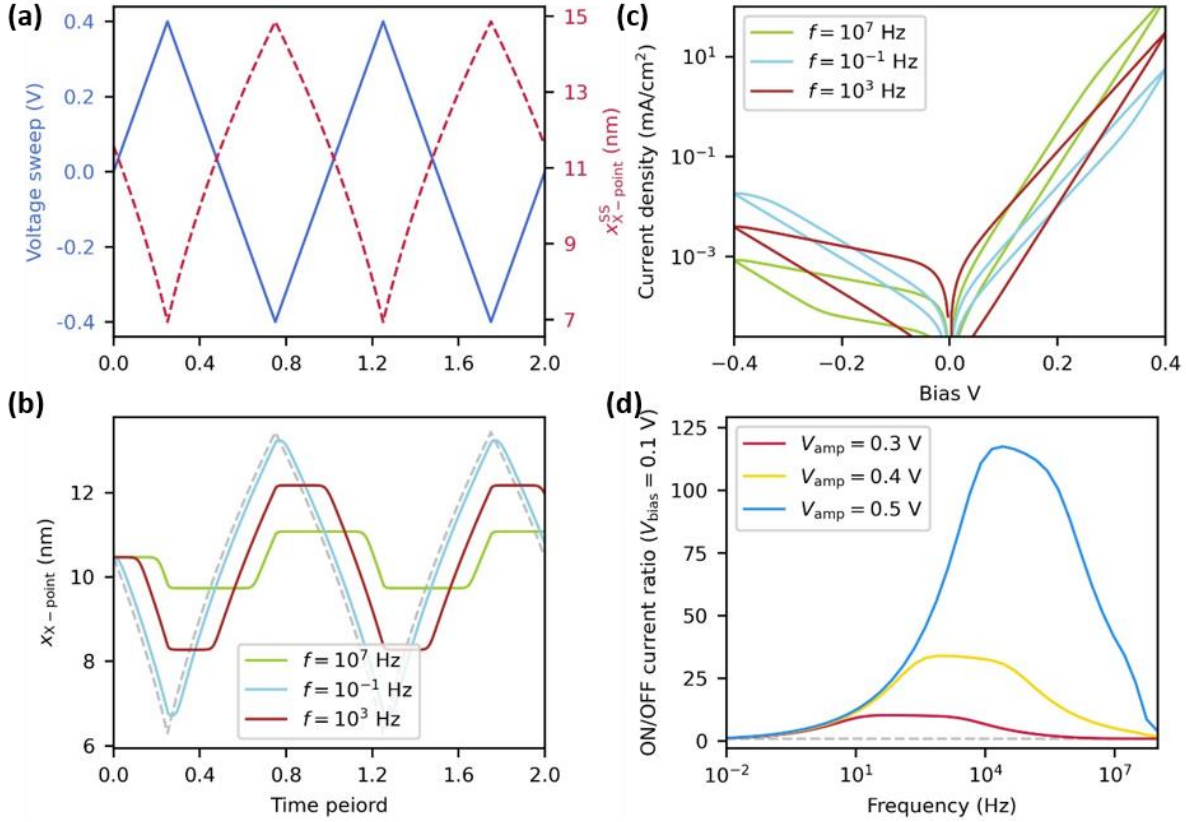


Figure 4: Modeling the dynamics of DLS resistive switching. (a) Change in $x_{X-point}^{SS}$ (the steady state value of $x_{X-point}$ for conditions of local equilibrium) for a triangle-wave applied bias. (b) Time-dependence of $x_{X-point}$ for three drive frequencies and a fixed drive amplitude of 0.4 V, as in (a). The dashed grey line traces $x_{X-point}^{SS}$, as in (a). (c) Simulated $I-V$ curves for three drive frequencies. We show only TFE, which dominates the junction current. (d) TFE current density on/off ratio at a bias of +0.1 V during one period of bias oscillation, as a function of drive frequency, for three different drive amplitudes (V_{amp}). Calculations shown for $N_t = 5 \times 10^{18} \text{ cm}^{-3}$, $E_{switch} = 0.8 \text{ eV}$, and $E_C - E_{trans} = 0.35 \text{ eV}$.

We also analyze the time-dependent response of the heterojunction to an abrupt step change in bias. The movement of $x_{X-point}$ after a change from 0 V to V_{step} at time $t = 0$ is described by:

$$x_{X-point}(t) - x_{X-point}^{SS} = \frac{k_B T}{k_{TR}} \operatorname{arctanh} \left(\tanh \left(\frac{2V_{step} - 2E_{trans,0}}{k_B T} \right) \exp \left(-\frac{t}{\tau_1} \right) \right) \quad (8)$$

$x_{X-point}^{SS}$ is the steady-state value of $x_{X-point}$ for bias V_{step} , k_{TR} is the derivative of the metastable transition energy versus the coordinate of the cross point (which is equal to dE_C/dx), $E_{trans,0}$ the value of E_{trans} at the initial coordinate $x_{X-point}(t = 0)$, τ_1 the time constant of the first order decay mode (see Appendix for details). Eqn. 9 means that $x_{X-point}$ will move towards $x_{X-point}^{SS}$ and $x_{X-point}(t \rightarrow \infty) = x_{X-point}^{SS}$. The $\operatorname{arctanh}$ function is highly nonlinear. After a Taylor expansion, we find:

$$x_{\text{X-point}}(t) - x_{\text{X-point}}^{\text{SS}} = \sum_{n=1}^{\infty} s_n \exp\left(-\frac{t}{\tau_n}\right), \quad \begin{cases} s_n = \frac{k_B T \left(\tanh\left(\frac{V_{\text{step}} - E_{\text{trans},0}}{k_B T}\right) \right)^{2n-1}}{k_{TR} (2n-1)} \\ \tau_n = \frac{\tau_1}{2n-1} \end{cases} \quad (9)$$

s_n and τ_n denotes the strength and time constant of the n -th order exponential term, respectively; s_n has units of length and it represents n -th order decay length. At short times $t \ll \tau_1$, the decay is dominated by high orders with time constants $\tau_n \ll \tau_1$. As we show in **Fig. 5a**, the initial change after $t = 0$ is sharp, being the sum of multiple exponential functions with short time constants. At later time $t \approx \tau_1$, only the first order exponential remains and it dominates the long-time dynamics. We find that τ_1 is nearly independent of V_{step} : for the parameters studied here, $\tau_1 \approx 0.6$ s for all $V_{\text{step}} = +0.1, +0.2$, and $+0.3$ V. In **Fig. 5b** we plot the time-dependence of the TFE current density, which qualitatively resembles the behavior of $x_{\text{X-point}}$.

The amplitude of V_{step} may not strongly affect τ_1 , but it does have a strong influence on dynamics at short times $t \ll \tau_1$. In **Fig. 5c** we present the lengths scales $s_n(\tau_n)$ for $V_{\text{step}} = +0.1, +0.2$, and $+0.3$ V. As V_{step} increases, the higher-order length scales increase significantly, corresponding to a faster change in the spatial distribution of N_{shallow} and N_{deep} and faster resistive switching. In **Fig. 5d** we show the cumulative sum of s_n with increasing time t , $\sum_{\tau_n < t} s_n(\tau_n)$. As we increase V_{step} , the short-time decay modes contribute more to the final displacement of $x_{\text{X-point}}$.

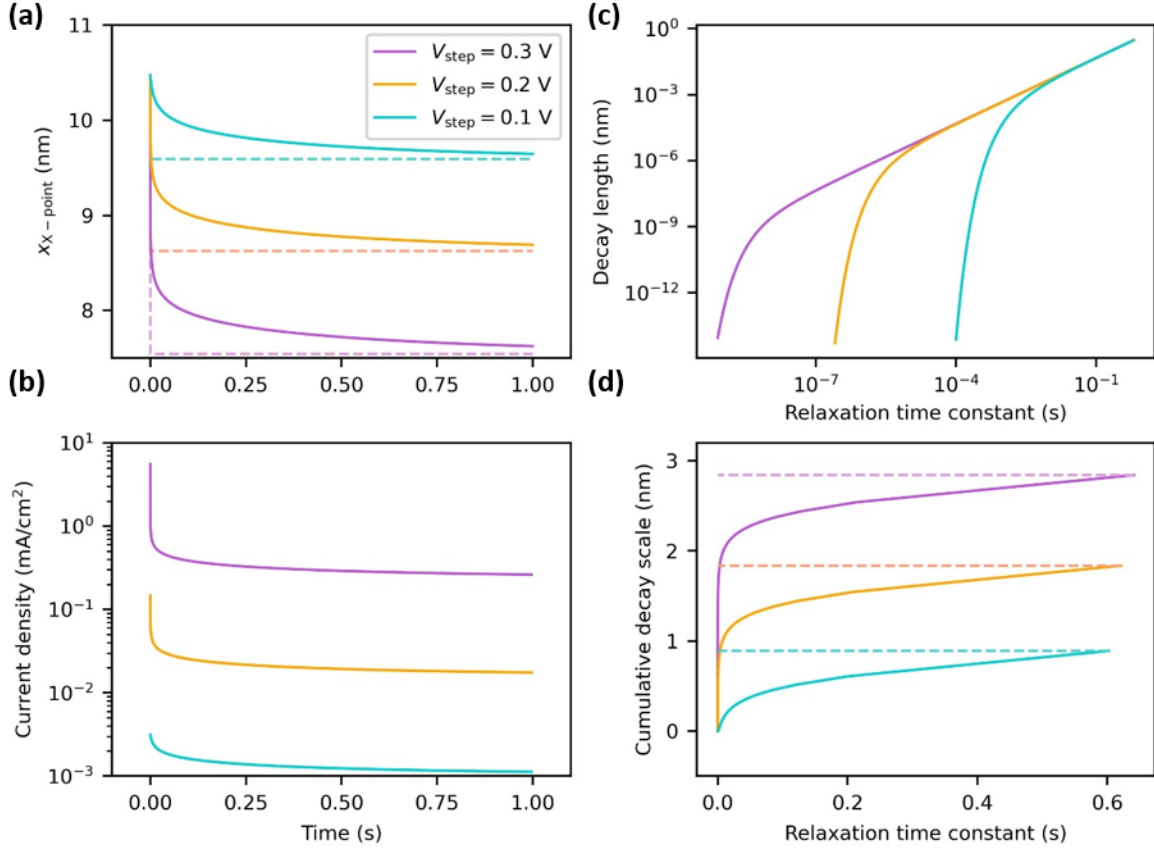


Figure 5: Analyzing the short-time response to a sudden change in bias from 0 to V_{step} . (a) $x_{X\text{-point}}(t)$ under the step pulse $V_{\text{step}} = +0.1, +0.2$, and $+0.3$ V, respectively. Dashed lines indicate $x_{X\text{-point}}^{\text{SS}}$. (b) Time evolution of the TFE current density. (c) $s_n(\tau_n)$, dependency of decay length on the relaxation time constant, showing the effect of increasing V_{step} in accelerating the short-time response. (d) $\sum_{\tau_n < \tau} s_n(\tau_n)$, cumulative decay length vs. relaxation time constant. Calculations shown for $N_t = 5 \times 10^{18} \text{ cm}^{-3}$, $E_C - E_{\text{trans}} = 0.35 \text{ eV}$, and $E_{\text{switch}} = 0.8 \text{ eV}$.

4. Effect of varying material parameters

In Sec. 2-3 we presented results for devices based on CdS, following our experimental demonstration.¹ CdS is one of many semiconductors featuring DLS-active defects, and we expect that similar devices physics can be realized in many other materials including ZnO, CuInSe₂, CuGaSe₂, and III-V materials featuring DX-centers.^{4,5,7,9} In each case, material parameters will differ from those of CdS (*e.g.*, see **Table S1**), but we found that only select parameters have strong influence on predicted DLS-based resistive switching. For instance, we find very weak dependence of the predicted behavior on the dielectric constant and effective mass. Here we highlight three parameters that do strongly influence device performance: the Schottky barrier height (Φ_{SBH}), the characteristic activation energy for defect level switching (E_{switch}), and the position of the switching energy level in the band gap ($E_C - E_{\text{trans}}$).

In **Fig. 6** we present the current density on/off ratio at a bias of +0.1 V during one period of bias oscillation, as a function of drive frequency for three values of Φ_{SBH} , with fixed values for $E_{\text{switch}} = 0.8$ eV, $E_{\text{C}} - E_{\text{trans}} = 0.35$ eV, and drive amplitude $V_{\text{amp}} = 0.4$ V. Varying Φ_{SBH} most strongly affects the amplitude of the on/off ratio because it affects the magnitude of TFE. For small Φ_{SBH} , the TFE current is large (due to the narrow depletion region), and the DLS switching effect is enhanced. As Φ_{SBH} increases, the depletion region becomes wider, and tunneling becomes less prominent, reducing the DLS switching effect. The bandwidth is less affected because it is determined primarily by E_{switch} , as shown below.

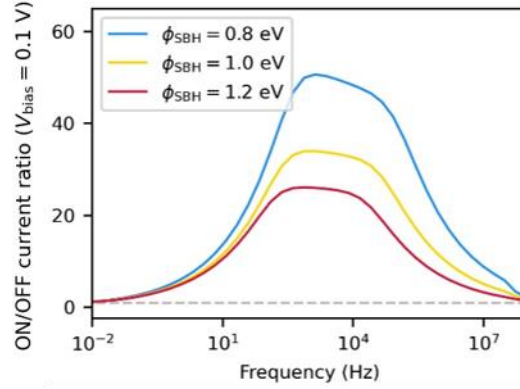


Figure 6: Effect of varying Φ_{SBH} on the current on/off ratio for fixed $E_{\text{switch}} = 0.8$ eV, $E_{\text{C}} - E_{\text{trans}} = 0.35$ eV, $N_{\text{t}} = 5 \times 10^{18} \text{ cm}^{-3}$, and drive amplitude $V_{\text{amp}} = 0.4$ V.

Like varying Φ_{SBH} , varying $E_{\text{C}} - E_{\text{trans}}$ primarily affects the on/off ratio, leaving the bandwidth unaffected, as we show in **Fig. 7**. This is because varying the position E_{trans} in the band gap affects the range within which $x_{\text{X-point}}$ varies. For a fixed value of Φ_{SBH} , a larger value of $E_{\text{C}} - E_{\text{trans}}$ (E_{trans} deeper in the gap) means that $x_{\text{X-point}}$ will be closer to the junction, and therefore has a stronger effect on the tunneling current density.

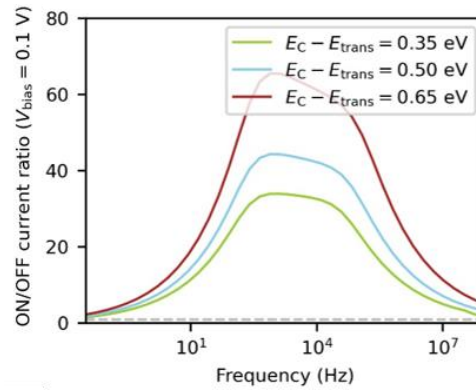


Figure 7: Effect of varying $E_{\text{C}} - E_{\text{trans}}$ on the current on/off ratio for fixed $\Phi_{\text{SBH}} = 0.8$ eV, $E_{\text{switch}} = 0.8$ eV, $N_{\text{t}} = 5 \times 10^{18} \text{ cm}^{-3}$, and drive amplitude $V_{\text{amp}} = 0.4$ V.

The bandwidth is controlled primarily by E_{switch} . In **Fig. 8** we present the results of varying E_{switch} on the on/off ratio for fixed values of $\Phi_{\text{SBH}} = 0.8$ eV, $E_{\text{switch}} = 0.8$ eV, and drive

amplitude $V_{\text{amp}} = 0.4$ V. For the three cases simulated, the time variation of $\chi_{\text{X-point}}^{\text{SS}}$ with applied bias is the same; the difference is the speed with which the system can follow the bias. E_{switch} is related to the enthalpy barrier for switching, which originates in the lattice distortions needed to transition between deep-donor and shallow-donor configurations (**Fig. 1b**). The shift in bandwidth can be understood simply in terms of the Arrhenius rate equation: the likelihood of finding an atomic rearrangement within a given time window decreases exponentially with the corresponding activation energy.

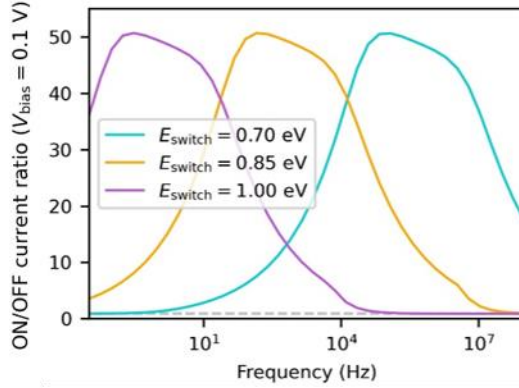


Figure 8: Effect of varying E_{switch} on the current on/off ratio for fixed $\Phi_{\text{SBH}} = 0.8$ eV, $E_C - E_{\text{trans}} = 0.35$ V, $N_t = 5 \times 10^{18} \text{ cm}^{-3}$, and drive amplitude $V_{\text{amp}} = 0.4$ V.

Summarizing this section, DLS device behavior is most strongly affected by the Schottky barrier height (Φ_{SBH}), the characteristic activation energy for defect level switching (E_{switch}), and the position of the switching energy level in the band gap ($E_C - E_{\text{trans}}$). These parameters can be varied through materials selection and defect engineering, with guidance from first-principles calculations and existing, sizable resources of empirical data on Schottky barrier heights and deep levels in compound semiconductors.

5. Discussion and conclusion

Being based on point defect charge state transitions, DLS devices are amenable to reliable simulation and technology computer-aided design (TCAD) to a greater extent than resistive switching technologies based on more physically-complex phenomena. The normally-on (*i.e.*, high conductivity at zero bias at equilibrium) devices studied here are completely unlike resistive switching devices being developed today for non-volatile memory and analog neuromorphic computing. We suggest that DLS devices may first find application in different settings. Gunn diodes are normally-on resistive switches that are a mainstay for microwave resonators. By analogy to Gunn diodes, DLS devices may be useful as resonators in the kHz-to-MHz range, with the added benefit that the device properties could be changed with controlled introduction of select defects (*i.e.*, doping), which is not possible with Gunn diodes. More speculatively, the dynamical range of DLS devices may find use in concepts for analog neuromorphic computing, such as in physical reservoir computing, and circuits featuring neural plasticity to combine on-the-fly training and data pre-processing. The availability of computational databases of the properties of defects in semiconductors, combined with the advent of reliable theoretical predictions of capture kinetics,

and TCAD simulations such as those developed here, suggests a future in which circuits employing DLS devices could be optimized through an inverse design process: first by identifying the circuit dynamics that best suit the proposed algorithm, then resolving dynamics to the level of individual devices, and then achieving the desired device dynamics by materials selection.

Our results highlight the tradeoff between bandwidth and conductivity on/off ratio that are inherent to resistive switching devices based on point defect charge state transitions. Earlier work by Schroeder *et al.* explored a phenomenon with some similarities: the “voltage-time dilemma” of proposed non-volatile memory based on charge storage at deep levels.⁸ In that setting, there is a tradeoff between the voltage needed to address individual bits and the retention time needed for non-volatile memory. The situation considered here is different in that we are studying bistable, DLS-active defects with deep- and shallow-donor configurations, instead of fixed deep levels, and we are explicitly interested in high-frequency response. Nevertheless, both studies explore the design space of resistive switching technologies based on immobile point defects, as opposed to technologies based on mass transport or phase transformations.

We suggest several directions for future work. It would be helpful to see DLS devices demonstrated experimentally in a materials system other than CdS. It would also be interesting to design and test DLS devices that are normally-off (like conventional resistive switches), so that both inhibitory and excitatory responses could be realized.

Acknowledgments

This work was supported by the Office of Naval Research MURI through Grant No. N00014-17-1-2661.

References

- ¹ H. Yin, A. Kumar, J.M. LeBeau, and R. Jaramillo, *Phys. Rev. Applied* **15**, 014014 (2021).
- ² G. Tanaka, T. Yamane, J.B. Héroux, R. Nakane, N. Kanazawa, S. Takeda, H. Numata, D. Nakano, and A. Hirose, *Neural Networks* **115**, 100 (2019).
- ³ D.V. Lang and R.A. Logan, *Phys. Rev. Lett.* **39**, 635 (1977).
- ⁴ S.B. Zhang, S.-H. Wei, and A. Zunger, *Phys. Rev. B* **63**, 075205 (2001).
- ⁵ S. Lany and A. Zunger, *Phys. Rev. B* **72**, 035215 (2005).
- ⁶ H. Yin, A. Akey, and R. Jaramillo, *Phys. Rev. Materials* **2**, 084602 (2018).
- ⁷ L. Gordon, J.L. Lyons, A. Janotti, and C.G. Van de Walle, *Phys. Rev. B* **89**, 085204 (2014).
- ⁸ H. Schroeder, V.V. Zhirnov, R.K. Cavin, and R. Waser, *Journal of Applied Physics* **107**, 054517 (2010).
- ⁹ P.M. Mooney, *Journal of Applied Physics* **67**, R1 (1990).
- ¹⁰ D.K. Schroder, *Semiconductor Material and Device Characterization*, 3rd ed (Wiley-IEEE Press, Piscataway, NJ : Hoboken, N.J, 2006).
- ¹¹ G. Chicot, P. Muret, J.-L. Santailler, G. Feuillet, and J. Pernot, *J. Phys. D: Appl. Phys.* **47**, 465103 (2014).
- ¹² S. Ababou, J.J. Marchand, L. Mayet, G. Guillot, and F. Mollot, *Superlattices and Microstructures* **7**, 283 (1990).
- ¹³ K. Decock, P. Zabierowski, and M. Burgelman, *Journal of Applied Physics* **111**, 043703 (2012).

¹⁴ S.M. Sze and K.K. Ng, *Physics of Semiconductor Devices (3rd Edition)*, 3rd ed. (Wiley-Interscience, Hoboken, N.J., 2006).

¹⁵ W.A. Harrison, *Phys. Rev.* **123**, 85 (1961).

¹⁶ R. Stratton, *Journal of Physics and Chemistry of Solids* **23**, 1177 (1962).

Appendices

A1. Material parameters

In **Table S1** we list the material parameters that we use to simulate DLS resistive switching devices based on CdS, ZnO, and n-AlGaAs:Si. DLTS shows a giant electron capture cross section, approximately 10^{-13} cm^2 , for DLS-active defects in ZnO and n-AlGaAs:Si.^{11,12} The electron cross section of DLS-active defects (*i.e.*, sulfur vacancies) in CdS has not been reported in the literature. We assume that it is comparable to that for ZnO and n-AlGaAs:Si. Our results are weakly sensitive to the semiconductor dielectric constant and electron effective mass, and therefore we use the values for CdS for all simulations. The Schottky barrier heights (ϕ_{Bn}) calculated for junctions between MoO₃ and the semiconductors CdS, ZnO, and n-AlGaAs:Si using the Schottky-Mott rule are unrealistically large, due to the myriad of effects summarized by Fermi level pinning. For a more realistic approximation of experiments, we simply use $\phi_{\text{Bn}} = 1 \text{ eV}$ everywhere unless otherwise stated.

| Material | $\sigma_n \text{ (cm}^2\text{)}$ | $E_{\text{trans}} \text{ (eV)}$ | $E_{\text{gap}} \text{ (eV)}$ | $\chi \text{ (eV)}$ | ϵ_r | m_e^* | $\mu_e \text{ (cm}^2\text{/V} \cdot \text{s)}$ |
|---|----------------------------------|---------------------------------|-------------------------------|---------------------|--------------|---------|--|
| CdS | $\sim 10^{-13}$ | 0.9 | 2.42 | 3.8~4.8 | 8.5 | 0.21 | 1.57 |
| ZnO | | 1.0 | 3.37 | 4.1~4.5 | 12.33 | 0.23 | ~205 |
| Al _x Ga _{1-x} As ($x=0.2$) | | 0.4 | 1.67 | 3.85 | 8.9 | 0.08 | ~4000 |

Table S1: Parameters used in simulations. σ_n is the electron capture cross section of DLS-active defects, E_{trans} is the metastable defect transition energy, E_{gap} is the band gap (not directly used in these simulations), χ is the electron affinity, ϵ_r is the relative dielectric constant, m_e^* is the effective electron mass, and μ_e is the electron mobility.

A2. Partial differential equations used in full band diagram simulations

For full simulation of the band diagram, we solve the Poisson equation and the drift-diffusion equation using the finite element method. The Poisson equation and its discrete differential expression are given by:

$$\epsilon \frac{\partial^2 \psi}{\partial x^2} = q(n - N_{\text{defect}}^+)$$

$$\psi_i = \frac{\psi_{i+1} + \psi_{i-1}}{2} - \frac{(\Delta L)^2 q}{2\epsilon} (n_i - N_{\text{defect},i}^+)$$

ψ_i denotes the electric potential at grid point i , ΔL is the grid spacing, ϵ is the semiconductor dielectric constant, n_i is the electron density at grid point i , and $N_{\text{defect},i}^+$ is the charge density of ionized defects at grid point i . The boundary conditions of the Poisson equation and the corresponding discrete differential expressions are:

$$\psi_{x=0} = -\frac{\phi_{Bn}}{q}, \quad \psi_{x=\infty} = -\left(\frac{\phi_n}{q} + V_{bias}\right)$$

$$\psi_{i=0} = -\frac{\phi_{Bn}}{q}, \quad \psi_{i=N_{mesh}-1} = -\left(\frac{\phi_n}{q} + V_{bias}\right)$$

ϕ_{Bn} is the Schottky barrier height, ϕ_n is the difference between the conduction band edge and the electron Fermi energy E_{Fn} in the quasi-neutral region (*i.e.*, far from the junction), N_{mesh} is the grid point number, and V_{bias} is the voltage applied across the heterojunction. Under these boundary conditions, the conduction edge band energy (E_C) is the negative of electric potential: $E_C = -q\psi$.

The equation for diffusion current density (J_D) is:

$$J_D = q\mu_n n \xi + qD_n \frac{\partial n}{\partial x} = \mu_n n \frac{\partial E_{Fn}}{\partial x}$$

μ_n is the electron mobility, D_n is the electron diffusivity, and ξ is the electric field (a scalar quantity in our one-dimensional model). Without considering the tunneling current, the diffusion current must be constant throughout the semiconductor.

We now derive a differential expression for E_{Fn} . The conduction electron density is:

$$n = N_C e^{\frac{-E_C + E_{Fn}}{k_B T}} = N_C e^{\frac{q\psi + E_{Fn}}{k_B T}}$$

N_C is effective density of state of the conduction band. We rewrite J_D as:

$$J_D = \mu_n N_C e^{\frac{q\psi + E_{Fn}}{k_B T}} \frac{\partial E_{Fn}}{\partial x} = \mu_n N_C k_B T e^{\frac{q\psi}{k_B T}} \frac{\partial e^{\frac{E_{Fn}}{k_B T}}}{\partial x}$$

This yields:

$$\frac{\partial e^{\frac{E_{Fn}}{k_B T}}}{\partial x} = \frac{J_D}{\mu_n N_C k_B T} e^{-\frac{q\psi}{k_B T}}$$

Assuming that ψ changes linearly between grid points i and $i+1$ (*i.e.*, $\psi(x_i \leq x \leq x_{i+1}) = \psi_i + (x - x_i)(\psi_{i+1} - \psi_i)/\Delta L$), integrating both sides of the above equation yields:

$$\frac{J_D}{\mu_n N_C k_B T} \frac{1}{-\frac{q}{k_B T} \frac{\psi_{i+1} - \psi_i}{\Delta L}} \left(e^{-\frac{q\psi_{i+1}}{k_B T}} - e^{-\frac{q\psi_i}{k_B T}} \right) = e^{\frac{E_{Fn,i+1}}{k_B T}} - e^{\frac{E_{Fn,i}}{k_B T}}$$

This yields:

$$J_D = \mu_n N_C \frac{-q\psi_{i+1} - (-q\psi_i)}{\Delta L} \frac{e^{\frac{E_{Fn,i+1}}{k_B T}} - e^{\frac{E_{Fn,i}}{k_B T}}}{e^{-\frac{q\psi_{i+1}}{k_B T}} - e^{-\frac{q\psi_i}{k_B T}}}$$

$$= \mu_n N_C \frac{k_B T}{\Delta L} \frac{\left(-\frac{q\psi_{i+1}}{k_B T}\right) - \left(-\frac{q\psi_i}{k_B T}\right)}{e^{-\frac{q\psi_{i+1}}{k_B T}} - e^{-\frac{q\psi_i}{k_B T}}} \left(e^{\frac{E_{Fn,i+1}}{k_B T}} - e^{\frac{E_{Fn,i}}{k_B T}}\right)$$

We denote J_D as $J_{D,i+1/2}$ because it's calculated from ψ_i , $E_{Fn,i}$, ψ_{i+1} , and $E_{Fn,i+1}$. Without considering tunneling current, the diffusion current must be continuous everywhere (i.e., $J_{D,i-1/2} = J_{D,i+1/2}$), yielding:

$$\frac{\left(-\frac{q\psi_i}{k_B T}\right) - \left(-\frac{q\psi_{i-1}}{k_B T}\right)}{e^{-\frac{q\psi_i}{k_B T}} - e^{-\frac{q\psi_{i-1}}{k_B T}}} \left(e^{\frac{E_{Fn,i}}{k_B T}} - e^{\frac{E_{Fn,i-1}}{k_B T}}\right) = \frac{\left(-\frac{q\psi_{i+1}}{k_B T}\right) - \left(-\frac{q\psi_i}{k_B T}\right)}{e^{-\frac{q\psi_{i+1}}{k_B T}} - e^{-\frac{q\psi_i}{k_B T}}} \left(e^{\frac{E_{Fn,i+1}}{k_B T}} - e^{\frac{E_{Fn,i}}{k_B T}}\right)$$

This yields a differential expression for $e^{\frac{E_{Fn,i}}{k_B T}}$:

$$e^{\frac{E_{Fn,i}}{k_B T}} = \frac{\frac{\left(-\frac{q\psi_i}{k_B T}\right) - \left(-\frac{q\psi_{i-1}}{k_B T}\right)}{e^{-\frac{q\psi_i}{k_B T}} - e^{-\frac{q\psi_{i-1}}{k_B T}}} e^{\frac{E_{Fn,i-1}}{k_B T}} + \frac{\left(-\frac{q\psi_{i+1}}{k_B T}\right) - \left(-\frac{q\psi_i}{k_B T}\right)}{e^{-\frac{q\psi_{i+1}}{k_B T}} - e^{-\frac{q\psi_i}{k_B T}}} e^{\frac{E_{Fn,i+1}}{k_B T}}}{\frac{\left(-\frac{q\psi_i}{k_B T}\right) - \left(-\frac{q\psi_{i-1}}{k_B T}\right)}{e^{-\frac{q\psi_i}{k_B T}} - e^{-\frac{q\psi_{i-1}}{k_B T}}} + \frac{\left(-\frac{q\psi_{i+1}}{k_B T}\right) - \left(-\frac{q\psi_i}{k_B T}\right)}{e^{-\frac{q\psi_{i+1}}{k_B T}} - e^{-\frac{q\psi_i}{k_B T}}}}$$

The corresponding boundary conditions are given by:

$$e^{\frac{E_{Fn,i=0}}{k_B T}} = 1, \quad e^{\frac{E_{Fn,i=N_{\text{mesh}}-1}}{k_B T}} = e^{\frac{qV_{\text{bias}}}{k_B T}}$$

Instead of calculating the Fermi energy directly, we calculate its exponential; then, after reaching self-consistency, we compute E_{Fn} from its exponential.

The differential expressions for ψ_i and $E_{Fn,i}$ are coupled:

$$\begin{cases} \psi_i = \frac{\psi_{i+1} + \psi_{i-1}}{2} - \frac{(\Delta L)^2}{2} \frac{q}{\varepsilon} \left(N_C e^{\frac{q\psi_i + E_{Fn,i}}{k_B T}} - N_{\text{defect},i}^+ \right) \\ e^{\frac{E_{Fn,i}}{k_B T}} = \frac{\frac{\left(-\frac{q\psi_i}{k_B T}\right) - \left(-\frac{q\psi_{i-1}}{k_B T}\right)}{e^{-\frac{q\psi_i}{k_B T}} - e^{-\frac{q\psi_{i-1}}{k_B T}}} e^{\frac{E_{Fn,i-1}}{k_B T}} + \frac{\left(-\frac{q\psi_{i+1}}{k_B T}\right) - \left(-\frac{q\psi_i}{k_B T}\right)}{e^{-\frac{q\psi_{i+1}}{k_B T}} - e^{-\frac{q\psi_i}{k_B T}}} e^{\frac{E_{Fn,i+1}}{k_B T}}}{\frac{\left(-\frac{q\psi_i}{k_B T}\right) - \left(-\frac{q\psi_{i-1}}{k_B T}\right)}{e^{-\frac{q\psi_i}{k_B T}} - e^{-\frac{q\psi_{i-1}}{k_B T}}} + \frac{\left(-\frac{q\psi_{i+1}}{k_B T}\right) - \left(-\frac{q\psi_i}{k_B T}\right)}{e^{-\frac{q\psi_{i+1}}{k_B T}} - e^{-\frac{q\psi_i}{k_B T}}}} \end{cases}$$

For full simulations, we solve these coupled equations cyclically. We make an initial guess for the distribution $E_{Fn,i}$, then iteratively calculate ψ_i until convergence. We then fix ψ_i , and iteratively calculate $E_{Fn,i}$ until convergence. We repeat this cycle until both distributions ψ_i and $E_{Fn,i}$ are converged, at which point the band diagram has reached self-consistency.

A3. Modeling DLS-active donor defects

For conventional donor-type defects, the space charge density is equal to the ionized defect density:

$$N_{\text{defect}}^+ = \frac{N_C \exp\left(\frac{-E_C + E_{\text{defect}}}{k_B T}\right)}{N_C \exp\left(\frac{-E_C + E_{\text{defect}}}{k_B T}\right) + n} N_{\text{defect}}$$

E_{defect} and N_{defect} are the donor defect transition energy level and concentration, respectively. DLS-active defects transform between shallow- and deep-donor configurations, with concentrations that we represent as N_{shallow} and N_{deep} , respectively. The total defect density N_t is fixed, and is the sum of N_{shallow} and N_{deep} :

$$N_{\text{shallow}} + N_{\text{deep}} = N_t$$

To calculate the space charge density of DLS-active donors, we count shallow donor and deep donor states separately. The shallow donors may be singly or doubly ionized, and we denote their concentration as N_{shallow}^{++} and N_{shallow}^+ , respectively (later we approximate them as always doubly ionized, $N_{\text{shallow}}^{++} = N_{\text{shallow}}$). The deep donors may be neutral or singly ionized, and we denote their concentration as N_{deep}^0 and N_{deep}^+ , respectively (later we approximate them as always neutral, $N_{\text{deep}}^0 = N_{\text{deep}}$). We can write the following relations:

$$\begin{aligned} N_{\text{shallow}} &= N_{\text{shallow}}^{++} + N_{\text{shallow}}^+, & N_{\text{shallow}}^{++} &= \frac{N_C \exp\left(\frac{-E_C + E_{\text{shallow}}}{k_B T}\right)}{N_C \exp\left(\frac{-E_C + E_{\text{shallow}}}{k_B T}\right) + n} N_{\text{shallow}} \\ N_{\text{deep}} &= N_{\text{deep}}^0 + N_{\text{deep}}^+, & N_{\text{deep}}^+ &= \frac{N_C \exp\left(\frac{-E_C + E_{\text{deep}}}{k_B T}\right)}{N_C \exp\left(\frac{-E_C + E_{\text{deep}}}{k_B T}\right) + n} N_{\text{deep}} \end{aligned}$$

To model the dynamics of defect level switching between shallow- and deep-donor configurations, we use a double capture/emission model that was developed to study persistent photoconductivity and related DLS phenomena in chalcopyrites.¹³ In this model, the single electron/hole capture/emission process are controlled by the following expressions:

$$\begin{aligned} \tau_{ec}^{-1} &= \sigma v_{rms} n = \sigma v_{rms} N_C \exp\left(\frac{-E_C + E_{Fn}}{k_B T}\right), & \tau_{ee}^{-1} &= \sigma v_{rms} N_C \\ \tau_{hc}^{-1} &= \sigma v_{rms} p = \sigma v_{rms} N_V \exp\left(\frac{-E_{Fn} + E_V}{k_B T}\right), & \tau_{he}^{-1} &= \sigma v_{rms} N_V \end{aligned}$$

τ_{ec}^{-1} , τ_{ee}^{-1} , τ_{hc}^{-1} and τ_{he}^{-1} denote the rates of single electron capture, single electron emission, single hole capture, and single hole emission, respectively. σ is the defect capture cross section, v_{rms} is the thermal velocity of electrons/holes, p is the free hole density, and N_V is the valence band

effective density of states. For simplicity, we assume that σ is constant for all four processes. We also assume that $N_C \approx N_V$ and that the electron and hole effective masses are equal, so that they have the same v_{rms} .

According to our understanding of DLS-active defects such as oxygen vacancies in ZnO (as illustrated in **Fig. 1**), we consider that the transformation between deep- and shallow-donor configurations is driven by double electron/hole processes. A neutral deep donor transforms into a doubly-ionized shallow donor by emitting two electrons/capturing two holes, accompanied by a large lattice relaxation. Likewise, a doubly-ionized shallow donor transforms into a neutral deep donor by capturing two electrons/emitting two holes. The double electron/hole capture/emission rates are given by:

$$\tau_{EC}^{-1} = \frac{1}{v_{\text{phonon}}} \tau_{ec}^{-1} \tau_{ec}^{-1} \exp\left(-\frac{\Delta E_{EC}}{k_B T}\right) \quad (\text{A1})$$

$$\tau_{EE}^{-1} = \frac{1}{v_{\text{phonon}}} \tau_{ee}^{-1} \tau_{ee}^{-1} \exp\left(-\frac{\Delta E_{EE}}{k_B T}\right) \quad (\text{A2})$$

$$\tau_{HC}^{-1} = \frac{1}{v_{\text{phonon}}} \tau_{hc}^{-1} \tau_{hc}^{-1} \exp\left(-\frac{\Delta E_{HC}}{k_B T}\right) \quad (\text{A3})$$

$$\tau_{HE}^{-1} = \frac{1}{v_{\text{phonon}}} \tau_{he}^{-1} \tau_{he}^{-1} \exp\left(-\frac{\Delta E_{HE}}{k_B T}\right) \quad (\text{A4})$$

τ_{EC}^{-1} , τ_{EE}^{-1} , τ_{HC}^{-1} and τ_{HE}^{-1} are the rates of double electron capture, double electron emission, double hole capture, and double hole emission, respectively. v_{phonon}^{-1} is an attempt frequency for the lattice relaxation. ΔE_{EC} , ΔE_{EE} , ΔE_{HE} and ΔE_{HC} are the activation energies for double electron capture, double electron emission, double hole emission and double hole capture, respectively. Eqn. A1-A4 account for the atomic lattice configuration changes that accompany defect level switching.

Now considering only double-electron (or double-hole) events, we have the following expressions for the time evolution of N_{shallow} and N_{deep} :

$$\begin{aligned} \frac{\partial N_{\text{shallow}}^{++}}{\partial t} &= -(\tau_{EC}^{-1} + \tau_{HE}^{-1})N_{\text{shallow}}^{++} + (\tau_{EE}^{-1} + \tau_{HC}^{-1})N_{\text{deep}}^0 \\ \frac{\partial N_{\text{deep}}^0}{\partial t} &= (\tau_{EC}^{-1} + \tau_{HE}^{-1})N_{\text{shallow}}^{++} - (\tau_{EE}^{-1} + \tau_{HC}^{-1})N_{\text{deep}}^0 \end{aligned}$$

When we apply a voltage bias to the junction, τ_{EC}^{-1} and τ_{HC}^{-1} are accelerated exponentially, while τ_{EE}^{-1} and τ_{HE}^{-1} remain unchanged because they are independent of the Fermi energy. Therefore, we consider τ_{EE}^{-1} and τ_{HE}^{-1} to be insignificant, yielding the following simplification:

$$\frac{\partial N_{\text{shallow}}^{++}}{\partial t} = -\tau_{EC}^{-1}N_{\text{shallow}}^{++} + \tau_{HC}^{-1}N_{\text{deep}}^0$$

$$\frac{\partial N_{\text{deep}}^0}{\partial t} = \tau_{EC}^{-1} N_{\text{shallow}}^{++} - \tau_{HC}^{-1} N_{\text{deep}}^0$$

Further manipulation yields:

$$\begin{aligned} \frac{\partial N_{\text{shallow}}^{++}}{\partial t} &= \frac{(\sigma v_{rms} N_C)^2}{v_{\text{phonon}}} \left\{ -\exp\left(\frac{-2E_C + 2E_{Fn} - \Delta E_{EC}}{k_B T}\right) N_{\text{shallow}}^{++} \right. \\ &\quad \left. + \exp\left(\frac{-2E_{Fn} + 2E_V - \Delta E_{EC}}{k_B T}\right) N_{\text{deep}}^0 \right\} \\ &= \frac{(\sigma v_{rms} N_C)^2}{v_{\text{phonon}}} \exp\left(-\frac{E_{\text{switch}}}{k_B T}\right) \left\{ -\exp\left(\frac{-2E_{Fn,TR} + 2E_{Fn}}{k_B T}\right) N_{\text{shallow}}^{++} \right. \\ &\quad \left. + \exp\left(\frac{2E_{Fn,TR} - 2E_{Fn}}{k_B T}\right) N_{\text{deep}}^0 \right\} \\ \frac{\partial N_{\text{deep}}^0}{\partial t} &= \frac{(\sigma v_{rms} N_C)^2}{v_{\text{phonon}}} \left\{ \exp\left(\frac{-2E_C + 2E_{Fn} - \Delta E_{EC}}{k_B T}\right) N_{\text{shallow}}^{++} \right. \\ &\quad \left. - \exp\left(\frac{-2E_{Fn} + 2E_V - \Delta E_{EC}}{k_B T}\right) N_{\text{deep}}^0 \right\} \\ &= \frac{(\sigma v_{rms} N_C)^2}{v_{\text{phonon}}} \exp\left(-\frac{E_{\text{switch}}}{k_B T}\right) \left\{ \exp\left(\frac{-2E_{\text{trans}} + 2E_{Fn}}{k_B T}\right) N_{\text{shallow}}^{++} - \exp\left(\frac{2E_{\text{trans}} - 2E_{Fn}}{k_B T}\right) N_{\text{deep}}^0 \right\} \end{aligned}$$

E_{switch} is a characteristic energy that determines the speed of defect level switching between deep- and shallow-donor configurations:

$$E_{\text{switch}} = E_C - E_V + \frac{1}{2}(\Delta E_{EC} + \Delta E_{HC}) \quad (\text{A5})$$

E_{trans} is the metastable transition energy level:

$$E_{\text{trans}} = \frac{E_V + E_C}{2} + \frac{\Delta E_{EC} - \Delta E_{HC}}{4} \quad (\text{A6})$$

In our model, E_{switch} and E_{trans} are determined solely by direct capture/emission between defects and conduction/valence band. In a realistic heterojunction, tunneling between defects and the conduction and valence bands will also contribute. Therefore, our simulations place a lower bound for the bandwidth of DLS-based resistive switching.

At steady state, under conditions of local equilibrium, N_{shallow} and N_{deep} are static in time, which yields:

$$\exp\left(\frac{-2E_{\text{trans}} + 2E_{Fn}}{k_B T}\right) N_{\text{shallow}}^{++} - \exp\left(\frac{2E_{\text{trans}} - 2E_{Fn}}{k_B T}\right) N_{\text{deep}}^0 = 0$$

From this we can derive the distributions of N_{shallow} and N_{deep} throughout the junction region.

A4. A simplified model of the depletion region

If all of the defects throughout the junction were fully ionized, then the conduction band energy would be written as:

$$E_C(x) = \phi_{Bn} - \frac{q^2 N_t}{\varepsilon} \left(L_{\text{full}} x - \frac{x^2}{2} \right)$$

$$L_{\text{full}} = \sqrt{\frac{2\varepsilon}{q^2 N_t} (\phi_{Bn} - \phi_n - qV_{\text{bias}})}$$

This is the conventional expression for a Schottky junction with uniform doping in the semiconductor. L_{full} is the depletion width (for the case of full defect ionization), ϕ_{Bn} is the Schottky barrier height, ϕ_n the difference between E_C and E_{Fn} in the quasi-neutral region (*i.e.*, far from the junction), and V_{bias} is the voltage applied across the heterojunction.

DLS-active defects are easily ionized in the shallow-donor configuration, but not so in the deep-donor configuration. Close to the junction, defects are likely ionized, shallow donors; far from the junction, they are likely neutral, deep donors. We define $x_{\text{X-point}}$ as the distance from the junction at which the concentrations of deep and shallow donors are equal, as shown in **Fig. 2c**. In a full solution, the ionization states of the deep and shallow donors vary continuously around $x_{\text{X-point}}$. As an approximation, to accelerate computation, we instead assume that the defect populations change abruptly at $x_{\text{X-point}}$:

$$N_{\text{shallow}}(x < x_{\text{X-point}}) = N_{\text{shallow}}^{++}(x > x_{\text{X-point}}) = N_t$$

$$N_{\text{deep}}(x > x_{\text{X-point}}) = N_{\text{deep}}^0(x > x_{\text{X-point}}) = N_t$$

At the cross point we have:

$$N_{\text{shallow}}(x = x_{\text{X-point}}) = N_{\text{shallow}}^{++}(x = x_{\text{X-point}}) = N_{\text{deep}}(x = x_{\text{X-point}}) = N_{\text{deep}}^0(x = x_{\text{X-point}}) = \frac{N_t}{2} \quad (\text{A7})$$

Using Gauss' theorem, we find that the electric potential varies quadratically for $x < x_{\text{X-point}}$ (as for a conventional Schottky junction) and linearly for $x > x_{\text{X-point}}$. We require that the potential vary smoothly at $x_{\text{X-point}}$, leading to the following expressions for $E_C(x)$:

$$E_{C,\text{quad}}(x < x_{\text{X-point}}) = \phi_{Bn} - \frac{q^2 N_t}{\varepsilon} \left(L_{\text{quad}} x - \frac{x^2}{2} \right)$$

$$E_{C,\text{linear}}(x > x_{\text{X-point}}) = \frac{q^2 N_t}{\varepsilon} (L_{\text{quad}} - x_{\text{cross}})(L_{\text{sample}} - x) + \phi_n + qV_{\text{bias}}$$

Equating $E_C(x)$ at the cross point, $E_{C,\text{quad}}(x = x_{\text{X-point}}) = E_{C,\text{linear}}(x = x_{\text{X-point}})$, we solve for L_{quad} and $E_C(x)$:

$$L_{\text{quad}} = x_{\text{X-point}} + \frac{L_{\text{full}}^2 - x_{\text{X-point}}^2}{2L_{\text{sample}}}$$

$$E_C(x) = \begin{cases} \phi_{Bn} - \frac{q^2 N_t}{\varepsilon} \left\{ \left(x_{\text{X-point}} + \frac{L_{\text{full}}^2 - x_{\text{X-point}}^2}{2L_{\text{sample}}} \right) x - \frac{x^2}{2} \right\}, & x < x_{\text{X-point}} \\ \frac{q^2 N_t}{\varepsilon} \frac{L_{\text{full}}^2 - x_{\text{X-point}}^2}{2L_{\text{sample}}} (L_{\text{sample}} - x) + \phi_n + qV_{\text{bias}}, & x > x_{\text{X-point}} \end{cases}$$

The metastable transition energy level $E_{Fn,TR}$ is below the conduction band energy E_C , and we define the difference between them as $\phi_{TR} = E_C - E_{Fn,TR}$. This yields an expression for $E_{Fn,TR}(x)$:

$$E_{Fn,TR}(x) = \begin{cases} \phi_{Bn} - \phi_{TR} - \frac{q^2 N_t}{\varepsilon} \left\{ \left(x_{\text{X-point}} + \frac{L_{\text{full}}^2 - x_{\text{X-point}}^2}{2L_{\text{sample}}} \right) x - \frac{x^2}{2} \right\}, & x < x_{\text{X-point}} \\ \frac{q^2 N_t}{\varepsilon} \frac{L_{\text{full}}^2 - x_{\text{X-point}}^2}{2L_{\text{sample}}} (L_{\text{sample}} - x) + \phi_n + qV_{\text{bias}} - \phi_{TR}, & x > x_{\text{X-point}} \end{cases}$$

At $x_{\text{X-point}}$, $E_{Fn,TR}$ is:

$$E_{Fn,TR}(x = x_{\text{X-point}}) = \frac{q^2 N_t}{\varepsilon} \frac{L_{\text{full}}^2 - x_{\text{X-point}}^2}{2L_{\text{sample}}} (L_{\text{sample}} - x_{\text{X-point}}) + \phi_n + qV_{\text{bias}} - \phi_{TR}$$

In steady-state conditions of local equilibrium at $x = x_{\text{X-point}}$, we have:

$$E_{Fn}(x = x_{\text{X-point}}) = E_{\text{trans}}(x = x_{\text{X-point}})$$

Sufficiently far from the top of the Schottky barrier, we have:

$$E_{Fn}(x = x_{\text{X-point}}) = E_{Fn}(x = L_{\text{sample}}) = qV_{\text{bias}}$$

This is a good approximation because E_{Fn} is flat almost everywhere in the depletion region; our simulations (*e.g.*, **Fig. 2a-b**) suggest that this approximation breaks down only within ≈ 2 nm of the junction, which is far less than $x_{\text{X-point}}$ for all simulations and results presented here.

Therefore, $x_{\text{X-point}}$ at steady-state conditions of local equilibrium, $x_{\text{X-point}}^{\text{SS}}$, is the solution of the equation:

$$\frac{q^2 N_t}{\varepsilon} \frac{L_{\text{full}}^2 - x_{\text{X-point}}^{\text{SS}^2}}{2L_{\text{sample}}} (L_{\text{sample}} - x_{\text{X-point}}^{\text{SS}}) + \phi_n - \phi_{TR} = 0$$

This is a cubic equation that we solve numerically; its standard form is:

$$x_{\text{X-point}}^{\text{SS}^3} - L_{\text{sample}} x_{\text{X-point}}^{\text{SS}^2} - L_{\text{full}}^2 x_{\text{X-point}}^{\text{SS}} + L_{\text{sample}} \left(L_{\text{full}}^2 + \frac{2\varepsilon}{q^2 N_t} (\phi_n - \phi_{TR}) \right) = 0$$

A5. Equation of motion for $x_{\text{X-point}}$

When the applied bias is changed, it takes time for $x_{X\text{-point}}$ to move to the new steady-state position $x_{X\text{-point}}^{\text{SS}}$. With time-dependent bias, $x_{X\text{-point}}(t)$ and $x_{X\text{-point}}^{\text{SS}}(t)$ are both dynamical variables. Here we derive an equation of motion for $x_{X\text{-point}}$ to simulate these dynamics.

Motion of $x_{X\text{-point}}$ is driven by the kinetic transformation between shallow- and deep-donor configurations. We write the equation of motion as:

$$\frac{dx_{X\text{-point}}}{dt} = - \frac{\left(\frac{\partial N_{\text{deep}}}{\partial t}\right)_{x=x_{X\text{-point}}}}{\left(\frac{\partial N_{\text{deep}}}{\partial x}\right)_{x=x_{X\text{-point}}}}$$

Using the approximation described in **Sec. A4** (Eqn. A7), we find that at $x_{X\text{-point}}$ the time-variation of N_{shallow} and N_{deep} can be written as:

$$\begin{aligned} \left(\frac{\partial N_{\text{shallow}}}{\partial t}\right)_{x=x_{X\text{-point}}} &= - \frac{(\sigma v_{\text{rms}} N_C)^2 N_t}{\nu_{\text{phonon}}} \exp\left(-\frac{E_{\text{switch}}}{k_B T}\right) \sinh\left(\frac{2E_{Fn} - 2E_{Fn,TR}(x_{X\text{-point}})}{k_B T}\right) \\ \left(\frac{\partial N_{\text{deep}}}{\partial t}\right)_{x=x_{X\text{-point}}} &= \frac{(\sigma v_{\text{rms}} N_C)^2 N_t}{\nu_{\text{phonon}}} \exp\left(-\frac{E_{\text{switch}}}{k_B T}\right) \sinh\left(\frac{2E_{Fn} - 2E_{Fn,TR}(x_{X\text{-point}})}{k_B T}\right) \end{aligned}$$

Deriving the spatial partial derivatives is more difficult. We approximate these as equal to the case of equilibrium at zero bias:

$$\left(\frac{\partial N_{\text{deep}}}{\partial x}\right)_{x=x_{X\text{-point}}} = \left(\frac{\partial N_{\text{deep}}}{\partial x}\right)_{x=x_{X\text{-point}}^{\text{SS}}, V_{\text{bias}}=0} = \left(\frac{\partial N_{\text{deep}}}{\partial x}\right)_{\text{init}}$$

To solve for the distribution of N_{shallow} and N_{deep} at steady-state conditions of local equilibrium, we use the equation:

$$\exp\left(\frac{-2E_{Fn,TR} + 2E_{Fn}}{k_B T}\right) N_{\text{shallow}}^{++} - \exp\left(\frac{2E_{Fn,TR} - 2E_{Fn}}{k_B T}\right) N_{\text{deep}}^0 = 0$$

Using $N_{\text{shallow}} = N_{\text{shallow}}^{++}$ and $N_{\text{deep}} = N_{\text{deep}}^0$, we find:

$$\exp\left(\frac{-2E_{Fn,TR} + 2E_{Fn}}{k_B T}\right) N_{\text{shallow}} - \exp\left(\frac{2E_{Fn,TR} - 2E_{Fn}}{k_B T}\right) N_{\text{deep}} = 0$$

With $N_{\text{shallow}} + N_{\text{deep}} = N_t$, we find the steady-state distribution of deep donors:

$$(N_{\text{deep}})_{\text{init}} = \frac{N_t}{1 + \exp\left(\frac{4E_{Fn,TR} - 4E_{Fn}}{k_B T}\right)}$$

The spatial derivative is:

$$\left(\frac{\partial N_{\text{deep}}}{\partial x}\right)_{\text{init}} = \frac{N_t}{\left(1 + \exp\left(\frac{4E_{Fn,TR} - 4E_{Fn}}{k_B T}\right)\right)^2} \exp\left(\frac{4E_{Fn,TR} - 4E_{Fn}}{k_B T}\right) \frac{4}{k_B T} \left(-\frac{\partial E_{Fn,TR}}{\partial x}\right)_{\text{init}}$$

At the initial cross point, $x_{X\text{-point}, \text{init}}^{\text{SS}}$:

$$\left(\frac{\partial N_{\text{deep}}}{\partial x}\right)_{x=x_{X\text{-point}, \text{init}}^{\text{SS}}} = N_t \frac{1}{k_B T} \left(-\frac{\partial E_{Fn,TR}}{\partial x}\right)_{x=x_{X\text{-point}, \text{init}}^{\text{SS}}}$$

Further derivation yields:

$$\left(\frac{\partial N_{\text{deep}}}{\partial x}\right)_{x=x_{X\text{-point}, \text{init}}^{\text{SS}}} = \frac{N_t}{L_{\text{decay}}}, \quad L_{\text{decay}} = \frac{k_B T}{\phi_{Bn} - \phi_n} \frac{L_{\text{full}, \text{init}}^2}{L_{\text{full}, \text{init}}^2 - x_{X\text{-point}, \text{init}}^{\text{SS}}^2} L_{\text{sample}}$$

L_{decay} is a characteristic decay length of the deep donor distribution N_{deep} under steady-state conditions: N_{deep} changes between approximately 0 and N_t around $x = x_{X\text{-point}}^{\text{SS}}$ over a length of L_{decay} .

With the above, we have a complete equation of motion for $x_{X\text{-point}}$:

$$\frac{\partial x_{X\text{-point}}}{\partial t} = -L_{\text{decay}} \frac{(\sigma v_{\text{rms}} N_C)^2}{v_{\text{phonon}}} \exp\left(-\frac{E_{\text{switch}}}{k_B T}\right) \sinh\left(\frac{2E_{Fn} - 2E_{Fn,TR}(x_{X\text{-point}})}{k_B T}\right)$$

A6. Response of the heterojunction to a step change in applied bias

Here we derive equations describing the response of the heterojunction to a step change in applied bias. The band diagram and therefor the junction conductivity are determined by $x_{X\text{-point}}$, therefore we calculate the response of $x_{X\text{-point}}$. At $x_{X\text{-point}}$, the metastable transition energy $E_{Fn,TR}(x_{X\text{-point}})$ is:

$$E_{Fn,TR}(x_{X\text{-point}}) = \frac{q^2 N_t L_{\text{full}}^2 - x_{X\text{-point}}^2}{\varepsilon 2L_{\text{sample}}} (L_{\text{sample}} - x_{X\text{-point}}) + \phi_n + qV_{\text{bias}} - \phi_{TR}$$

After a change in V_{bias} at $t = 0$ from 0 to V_{step} , $x_{X\text{-point}}$ moves several nanometers from the initial coordinate, so we make the reasonable assumption that $E_{Fn,TR}(x_{X\text{-point}})$ changes linearly around the initial coordinate $x_{X\text{-point}}(t = 0) = x_{X\text{-point},0}$. Therefore:

$$E_{Fn,TR}(x_{X\text{-point}}) = E_{Fn,TR,0} - k_{TR}(x_{X\text{-point}} - x_{X\text{-point},0})$$

$$k_{TR} = \frac{\phi_{Bn} - \phi_n - qV_{\text{step}}}{L_{\text{sample}}} \left(1 + \frac{2x_{X\text{-point},0} L_{\text{sample}}}{L_{\text{full}}^2} - \frac{3x_{X\text{-point},0}^2}{L_{\text{full}}^2}\right)$$

$-k_{TR}$ is the derivative of the metastable transition energy $E_{Fn,TR}$ with respect to $x_{X\text{-point}}$. The equation of motion becomes:

$$\frac{\partial x_{X\text{-point}}}{\partial t} = -L_{\text{decay}} \frac{(\sigma v_{\text{rms}} N_C)^2}{v_{\text{phonon}}} \exp\left(-\frac{E_{\text{switch}}}{k_B T}\right) \sinh\left(\frac{2V_{\text{step}} - 2E_{\text{trans},0} + 2k_{TR}(x_{X\text{-point}} - x_{X\text{-point},0})}{k_B T}\right)$$

We separate variables as follows:

$$\frac{d \exp\left(\frac{2V_{\text{step}} - 2E_{\text{trans},0} + 2k_{TR}(x_{X\text{-point}} - x_{X\text{-point},0})}{k_B T}\right)}{\exp\left(\frac{4V_{\text{step}} - 4E_{\text{trans},0} + 4k_{TR}(x_{X\text{-point}} - x_{X\text{-point},0})}{k_B T}\right) - 1} = -\frac{k_{TR} L_{\text{decay}} (\sigma v_{\text{rms}} N_C)^2}{k_B T v_{\text{phonon}}} \exp\left(-\frac{E_{\text{switch}}}{k_B T}\right) dt \quad (\text{A8})$$

We simply by introducing new variable y :

$$y = \exp\left(\frac{2V_{\text{step}} - 2E_{\text{trans},0} + 2k_{TR}(x_{X\text{-point}} - x_{X\text{-point},0})}{k_B T}\right)$$

We rewrite Eqn. A8 as:

$$\frac{dy}{y^2 - 1} = -\frac{k_{TR} L_{\text{decay}} (\sigma v_{\text{rms}} N_C)^2}{k_B T v_{\text{phonon}}} \exp\left(-\frac{E_{\text{switch}}}{k_B T}\right) dt$$

It follows that:

$$dy \left(\frac{1}{y-1} - \frac{1}{y+1} \right) = -\frac{2k_{TR} L_{\text{decay}} (\sigma v_{\text{rms}} N_C)^2}{k_B T v_{\text{phonon}}} \exp\left(-\frac{E_{\text{switch}}}{k_B T}\right) dt$$

Integrating both sides, we have:

$$\ln \frac{y-1}{e^{\frac{2V_{\text{step}} - 2E_{\text{trans},0}}{k_B T}} - 1} - \ln \frac{y+1}{e^{\frac{2V_{\text{step}} - 2E_{\text{trans},0}}{k_B T}} + 1} = -\frac{2k_{TR} L_{\text{decay}} (\sigma v_{\text{rms}} N_C)^2}{k_B T v_{\text{phonon}}} \exp\left(-\frac{E_{\text{switch}}}{k_B T}\right) t$$

We simplify the left-hand side as:

$$\ln \frac{(y-1) \left(e^{\frac{2V_{\text{step}} - 2E_{\text{trans},0}}{k_B T}} + 1 \right)}{(y+1) \left(e^{\frac{2V_{\text{step}} - 2E_{\text{trans},0}}{k_B T}} - 1 \right)} = \ln \frac{\tanh\left(\frac{V_{\text{step}} - E_{\text{trans},0} + k_{TR}(x_{X\text{-point}} - x_{X\text{-point},0})}{k_B T}\right)}{\tanh\left(\frac{V_{\text{step}} - E_{\text{trans},0}}{k_B T}\right)}$$

This yields the solution:

$$\tanh\left(\frac{V_{\text{step}} - E_{\text{trans},0} + k_{TR}(x_{X\text{-point}} - x_{X\text{-point},0})}{k_B T}\right) = \tanh\left(\frac{V_{\text{step}} - E_{\text{trans},0}}{k_B T}\right) \exp\left(-\frac{2k_{TR} L_{\text{decay}} (\sigma v_{\text{rms}} N_C)^2}{k_B T v_{\text{phonon}}} \exp\left(-\frac{E_{\text{switch}}}{k_B T}\right) t\right)$$

The motion of $x_{\text{X-point}}$ is given by:

$$x_{\text{X-point}} = x_{\text{X-point},0} - \frac{V_{\text{step}} - E_{\text{trans},0}}{k_{TR}} + \frac{k_B T}{k_{TR}} \operatorname{arctanh} \left(\tanh \left(\frac{V_{\text{step}} - E_{\text{trans},0}}{k_B T} \right) \exp \left(- \frac{2k_{TR} L_{\text{decay}} (\sigma v_{\text{rms}} N_C)^2}{k_B T v_{\text{phonon}}} \exp \left(- \frac{E_{\text{switch}}}{k_B T} \right) t \right) \right)$$

The slowest relaxation time constant is:

$$\tau_1 = \left(\frac{2k_{TR} L_{\text{decay}} (\sigma v_{\text{rms}} N_C)^2}{k_B T v_{\text{phonon}}} \exp \left(- \frac{E_{\text{switch}}}{k_B T} \right) \right)^{-1}$$

With a Taylor expansion, we express the motion of $x_{\text{X-point}}$ as a series of exponentials in time with time constants τ_n and amplitudes s_n :

$$x_{\text{X-point}} = x_{\text{X-point},0} - \frac{V_{\text{step}} - E_{\text{trans},0}}{k_{TR}} + \sum_{n=1}^{\infty} s_n \exp \left(- \frac{t}{\tau_n} \right),$$

$$\begin{cases} s_n = \frac{k_B T}{k_{TR}} \frac{\left(\tanh \left(\frac{V_{\text{step}} - E_{\text{trans},0}}{k_B T} \right) \right)^{2n+1}}{2n-1} \\ \tau_n = \frac{\tau_1}{2n-1} \end{cases}$$

A7. Current transport mechanisms

We consider three mechanisms of current transport through the heterojunction: thermionic emission, diffusion, and thermionic field emission (TFE). For simplicity we consider only electron transport, appropriate for wide-band gap n -type semiconductors.

The diffusion current density J_{diff} is the product of electron mobility, electron density and Fermi energy gradient:

$$J_{\text{diff}} = \mu_n n \frac{\partial E_{Fn}}{\partial x}$$

In full simulations, we solve for J_{diff} using the finite element method in combination with the Poisson equation. After Sze and Ng, we can also write J_{diff} as:¹⁴

$$J_{\text{diff}} = \mu_n N_C \frac{k_B T \left(\exp \left(\frac{q V_{\text{bias}}}{k_B T} \right) - 1 \right)}{\int_0^{L_{\text{full}}} \exp \left(\frac{E_C(x)}{k_B T} \right) dx}$$

If we know the spatial variation of the conduction band energy $E_C(x)$ (equal here to the electric potential), then the diffusion current can be calculated. When all defects are ionized, the expression for $E_C(x)$ is quadratic (as for a conventional Schottky junction), and we have:

$$J_{\text{diff, full}} \approx \mu_n N_C \frac{\phi_{Bn} - \phi_n - qV_{\text{bias}}}{L_{\text{full}}} \exp\left(-\frac{\phi_{Bn}}{k_B T}\right) \left(\exp\left(\frac{qV_{\text{bias}}}{k_B T}\right) - 1\right)$$

J_{diff} is approximately inversely proportional to the depletion width, and L_{full} is the depletion width for this case of full defect ionization. This dependence on the size and shape of the depletion region is much weaker than that of the TFE current density, which makes diffusion current less useful for DLS-based resistive switching.

We write the sum of thermionic emission (TE) and TFE current density as:^{15,16}

$$J_{TFE} + J_{TE} = q \frac{4\pi m^*}{h^3} \int_0^\infty dE_n \frac{1}{1 + e^{\frac{E_n + \phi_n}{k_B T}}} \int_0^{E_n} dE_{nx} e^{-\frac{2\sqrt{2m^*}}{\hbar} \int_{\Phi_n(x_1) - E_{nx}=0}^{\Phi_n(x_2) - E_{nx}=0} \sqrt{\Phi_n(x) - E_{nx}} dx}$$

E_n is the electron energy measured from the conduction band edge, E_{nx} is the electron kinetic energy measured in the x -direction (perpendicular to the heterojunction), $\Phi_n(x)$ is the energy barrier for the electron in the depletion region (*i.e.*, $\Phi_n(x) = E_C(x) - (\phi_n + qV_{\text{bias}})$), and m^* is the electron effective mass. The Fermi distribution is in the first integral, and the barrier transparency is in the second integral.

Further derivation yields:

$$J_{TFE} + J_{TE} = q \frac{4\pi m^* (k_B T)^2}{h^3} \int_0^{\Phi_{n,\text{max}}} \frac{dE_{nx}}{k_B T} \ln\left(1 + e^{-\frac{E_{nx} + \phi_n}{k_B T}}\right) e^{-\frac{2\sqrt{2m^*}}{\hbar} \int_{\Phi_n(x) - E_{nx}=0}^{\Phi_n(x) - E_{nx}=0} \sqrt{\Phi_n(x) - E_{nx}} dx} + q \frac{4\pi m^* (k_B T)^2}{h^3} \int_{\Phi_{n,\text{max}}}^\infty \frac{dE_{nx}}{k_B T} \ln\left(1 + \exp\left(-\frac{E_{nx} + \phi_n}{k_B T}\right)\right)$$

$\Phi_{n,\text{max}}$ is the maximum electron energy barrier (*i.e.*, $\Phi_{n,\text{max}} = \phi_{Bn} - (\phi_n + qV_{\text{bias}})$). Thermionic emission corresponds to E_{nx} making the transparency equal to unity. Hence, we have:

$$J_{TFE} = q \frac{4\pi m^* (k_B T)^2}{h^3} \int_0^{\Phi_{n,\text{max}}} \frac{dE_{nx}}{k_B T} \ln\left(1 + e^{-\frac{E_{nx} + \phi_n}{k_B T}}\right) e^{-\frac{2\sqrt{2m^*}}{\hbar} \int_{\Phi_n(x) - E_{nx}=0}^{\Phi_n(x) - E_{nx}=0} \sqrt{\Phi_n(x) - E_{nx}} dx}$$

$$J_{TE} = q \frac{4\pi m^* (k_B T)^2}{h^3} e^{\frac{qV_{\text{bias}} - \phi_{Bn}}{k_B T}}$$

We calculate the current density from the above expressions after solving for the band diagram (by full numerical convergence, or using the approximation described above). We see that the tunneling current (J_{TFE}) is exponentially sensitive to the width of the energy barrier, whereas thermionic emission (J_{TE}) is insensitive to the shape of the depletion region.

We further rewrite the tunneling current as:

$$J_{TFE} = q \frac{4\pi m^* (k_B T)^2}{h^3} \int_0^{\Phi_{n,\max}} \frac{dE_{nx}}{k_B T} \ln \left(1 + e^{-\frac{E_{nx} + \phi_n}{k_B T}} \right) e^{-\frac{2\sqrt{2m^*}}{\hbar} \sqrt{\Phi_{n,\text{eff}}(E_{nx})} L_{n,\text{eff}}(E_{nx})}$$

$\Phi_{n,\text{eff}}(E_{nx})$ and $L_{n,\text{eff}}(E_{nx})$ are the effective barrier height and length for electrons with energy E_{nx} . When we switch the depletion width while leaving the barrier height unchanged, the tunneling current through the heterojunction changes exponentially, while the thermionic emission current remains constant. Therefore, only the tunneling current is useful for DLS-based resistive switching.